Modeling of the PGSS Process by Crystallization and Atomization

Jun Li, Miguel Rodrigues, Alexandre Paiva, Henrique A. Matos, and Edmundo Gomes de Azevedo
Dept. of Chemical Engineering, Instituto Superior Técnico, 1049-001 Lisbon, Portugal

DOI 10.1002/aic.10478
Published online May 26, 2005 in Wiley InterScience (www.interscience.wiley.com).

A particles from gas-saturated solution (PGSS) process for the model system hydrogenated palm oil (HPO) with CO_2 was implemented and particle information, including size, size distribution, and morphology, is reported. The PGSS process in a capillary nozzle is modeled to be in steady, one-dimensional, inviscid, and two-phase (CO_2-rich phase and liquid HPO/CO_2 phase) annular-mist flow. The Peng–Robinson equation of state is applied for the nonideality of the binary CO_2/HPO and the fluid hydrodynamic equations of two phases are established to describe the system's pressure, temperature, velocity, and density along the nozzle. The aerosol dynamic equation for the crystallization of HPO in the CO_2-rich phase is used to explain the HPO crystal formation and growth under supercooling and supersaturation. For the liquid HPO/CO_2 phase, the atomization mechanism in terms of the interaction of the two phases gives HPO droplet information. The coupled model equations are numerically solved to obtain the HPO particle size and particle size distribution at the nozzle exit under several operating conditions. Different distribution modes are found, in agreement with the experimentally obtained particle spectra, an indication of the soundness of the model's particle formation mechanisms. Particles produced by atomization usually prevail over those formed from crystallization; yet, there exist special operating conditions under which the rapid expansion of supercritical solution (RESS) mechanism cannot be neglected and melt crystallization may be significant. The comparison between theoretical and experimental particle morphologies indicates that atomization may produce mainly spherical but relatively large particles; melt crystallization provides amorphous crystal particles, and the RESS process gives small and irregular crystals. © 2005 American Institute of Chemical Engineers *AIChE J,* 51: 2343–2357, 2005

Keywords: PGSS, crystallization, atomization, particles, supercritical fluids

Introduction

The PGSS (particles from gas-saturated solutions) process is a promising technique that uses fluids at supercritical conditions to produce fine powders under mild operating conditions. In this technique, a supercritical fluid (SCF) is dissolved into a solution of a solute in a solvent or into a melted material. Then, by selecting the appropriate pressure and temperature conditions, this mixture is rapidly depressurized through a nozzle causing the formation of solid particles. The PGSS process takes advantage of the fact that a gas is more soluble in a liquid than the corresponding liquid is in the same gas and it requires lower amounts of the dense gas than the extensively studied RESS (rapid expansion of supercritical solutions) technique. In RESS the solute is first dissolved in a SCF and the corresponding mixture is expanded rapidly through a nozzle. This sudden depressurization lowers the solvent power of the compressed fluid causing the dissolved solute to precipitate in a fine dis-

Permanent address of J. Li: Dept. of Chemical and Biochemical Engineering, Xiamen University, Fujian, Xiamen 361005, China.
Correspondence concerning this article should be addressed to E. Gomes de Azevedo at egazevedo@ist.utl.pt.

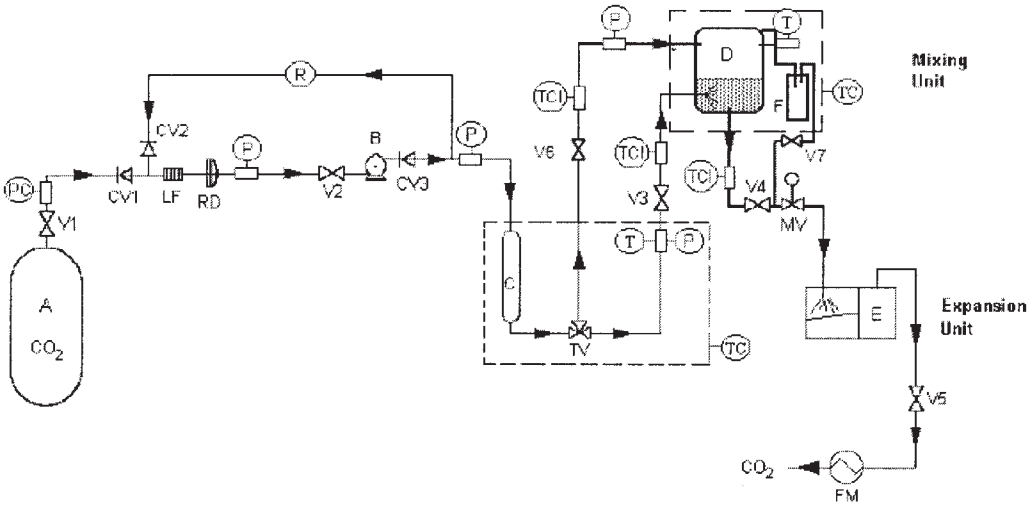

Figure 1. Apparatus used for the PGSS and RESS experiments.

A, CO_2 supply cylinder; B, gas compressor; C, CO_2 storage cylinder; D, mixing vessel; E, gas–solid separator; F, separation vessel; PC, pressure controller; TC, temperature controller; TCI, temperature controller and indicator; R, back-pressure regulator; P, pressure indicator; T, temperature indicator; LF, line filter; RD, rupture disc; V#, valve; CV#, check valve; TV, three-way valve; MV, micrometering valve; FM, flow meter.

persed form. Depending on nozzle design, temperature of mixture (before and in the nozzle), and pressure in the spray chamber, different forms of solids can be obtained, ranging from fine powders to crystalline needles or even thin films. Application of RESS is limited to those components that are appreciably soluble in the dense gas (carbon dioxide in most cases).

When the gas carries a dissolved drug or the drug is dissolved into the liquid before its expansion, the PGSS technique is particularly suited for the encapsulation of drugs into polymer or lipid matrices.[1] It is well known that the use of this technique has some limitations. For example, PGSS may give many spherical particles together with many smaller irregular-shaped crystals. The latter are not appropriate to be used in drug encapsulation processes because of the propagation of burst release kinetics. Particle size and particle size distribution mechanisms are not fully understood under given operating conditions. The PGSS process is far from being a custom-designed particle technique, required to adequately control particle sizes, their size distribution, and morphology. Therefore, particle design requires a complete comprehension of the mechanism that adequately describes the particle formation in the nozzle.

In previous works[2,3] we investigated separately the crystallization and atomization mechanisms for this process. The crystallization model was based on a two-phase homogeneous assumption to simplify the fluid dynamic equations of the complex system, and then the aerosol dynamic equation was used to describe the melt crystallization process of HPO in the supercooling pseudophase. This model could give information on the HPO particle size and particle size distribution at different preexpansion temperatures, preexpansion pressures, and nozzle dimensions. The simulation results could qualitatively account for some experimental evidence, such as the trend effect of the operating conditions on particle size and the particle morphology change around some special conditions. The atomization model, based on an annular two-phase flow, has shown that the velocity difference of the two phases may be large and that the liquid HPO phase could be atomized to form microdroplets that might be supported by a few large liquid droplets, similarly to what is experimentally observed when the preexpansion temperature is relatively high. Both models show similar trends for the dependency of the particle size on the preexpansion pressure, preexpansion temperature, and nozzle dimension. Nevertheless, those models could not provide enough information to attribute a unique mechanism to the PGSS process and could not conveniently predict the particle morphology and the particle size distribution at the nozzle exit. As shown later, in some experiments we obtained particles of different shapes and with bimodal-like size distributions. Two mechanisms may likely occur simultaneously in the PGSS process as a result of the different particle morphologies found in most of our experiments.

In this paper, we first introduce comprehensive experimental studies carried out with the PGSS process for the model system (CO_2/HPO) and the corresponding detailed information for the particles obtained, including their size, size distribution, and morphology. Second, we develop a general model based on the atomization and the crystallization mechanisms that considers both the melt crystallization and the gas-solution crystallization (a typical mechanism of the RESS process). Finally, we qualitatively compare the experimental with the simulated particle information. This comparison will support the discussions on the particle formation mechanism for our model system.

Experimental

Apparatus

Figure 1 shows the PGSS apparatus implemented for the model system HPO/CO_2. This apparatus is a slightly modified version of the apparatus described previously.[1] After the appropriate changes, the same apparatus was used for the RESS process.

Carbon dioxide (98% pure, supplied by Ar Líquido, Portugal) from the storage cylinder A is compressed (by the com-

pressor B) into the temperature-controlled storage vessel C and then to the mixing vessel D through a nozzle having an orifice diameter of 1.8 mm to mix with the liquid HPO previously loaded into vessel D. The mixed solution was then precipitated at constant temperature and pressure by rapid expansion to atmospheric pressure through a stainless steel tube (200 mm long) provided with an interchangeable nozzle with a laser-drilled orifice (diameter: 25–100 μm) to produce the desired particles. Particles were collected at ambient conditions in a clear gas–solid separator E, where a filter was installed to retain the HPO particles. After the precipitation, the CO_2 flow rate was measured and vented. For the RESS process, supercritical CO_2 was saturated with liquid HPO in the mixing vessel D and then withdrawn from the top of this vessel and fed into separation vessel F, with valves V4 and V6 closed, to ensure that no liquid HPO could be entrained by the gas stream. Then this HPO-saturated gas stream passed through valve V7 and micrometering valve MV and was expanded through the nozzle into the expansion unit.

Pressures were measured by pressure transducers (Setra, model 204) coupled to digital indicators (Setra, Datum-2001 model). The working pressure is controlled by a back-pressure regulator (Tescom, model 26-1722-24). Temperatures were measured by T-type thermocouples (Omega) with a six-channel digital indicator (Omega, model DP462-TC). The apparatus allows the independent control of all main process parameters, that is, preexpansion temperatures, mixing vessel pressure and temperature, disc orifice diameter, and SCF flow. The vegetable fat hydrogenated palm oil (HPO) is a high melting point lipid commonly used as a texturing and encapsulating agent for food products. It was supplied by Microlithe SA (France), had an average of 21–50% saturated fatty acids, an average of 39–59% monounsaturated fatty acids and of 10–19% linoleic acid (linolenic acid was about 0.3–0.9% and oleic acid 0.04%). The fatty acids were mainly C_{18}.

Particle morphology was analyzed by scanning electron microscopy (Hitachi, model S2400). Particle samples were previously coated with an averaged 15-nm gold film by electrodeposition in vacuum (Sputter Coater E5100). Particle samples were analyzed with a particle size analysis system consisting of an Aerosizer (TSI Inc., model LD) sensor unit for the determination of particle size and particle size distributions. The minimum detected particle size is 0.1 μm. All runs were carried out using more than 25,000 particles.

Particle sizes and particle size distributions

Microparticles were produced at different preexpansion temperatures (T_0), preexpansion pressures (P_0), and with two nozzles of different disc orifices (D = 25 μm and D = 100 μm). At least three different runs were performed for experiments at the same conditions (such as at fixed T_0, P_0, and D). Particle sizes and particle size distributions were then averaged for those similar runs.

Figures 2 and 3 give the experimental particle size distributions at different operating conditions. These figures show that particle sizes are slightly dependent on the operating conditions. In addition, they show that there exist bimodal distributions for the 25-μm diameter nozzle at intermediate preexpansion temperatures and pressures. Bimodal distributions can also be found for all cases in our previously reported results at T_0 = 359 K, D = 25 μm, and at different preexpansion pressures.[1] Yet, it usually gives a unimodal lognormal particle size distribution with low (or moderate) pressures or with low temperatures or with high nozzle diameters ($D \geq 100$ μm).

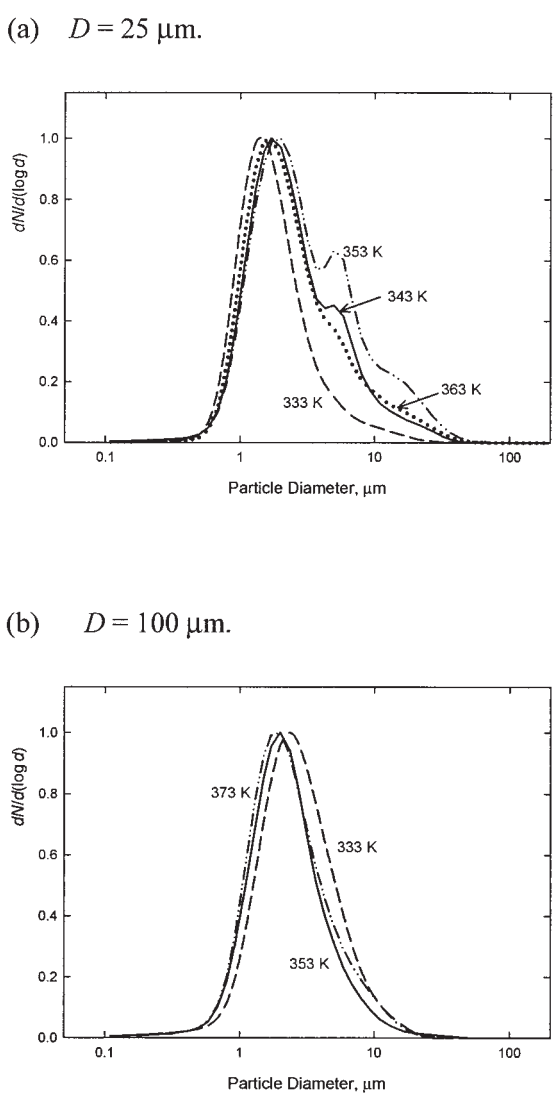

Figure 2. Experimental particle size distributions at P_0 = 16 MPa and different preexpansion temperatures for nozzles with: (a) D = 25 μm; (b) D = 100 μm.

Particle morphology information

For further analysis on the different mechanisms proposed here, Figure 4a–4d shows selected SEM microphotographs of HPO microparticles with different particle shapes, obtained with the 100-μm diameter nozzle.

These different particle shapes are mainly amorphous crystals or spheres. Figures 4a and 4b show that low preexpansion pressures produce some relatively large spheres together with small crystals, whereas high pressures produce an abundance of relatively small spheres and crystals. Figures 4c and 4d show that low preexpansion temperatures produce many crystals and few (but large) spheres, and that high temperatures produce

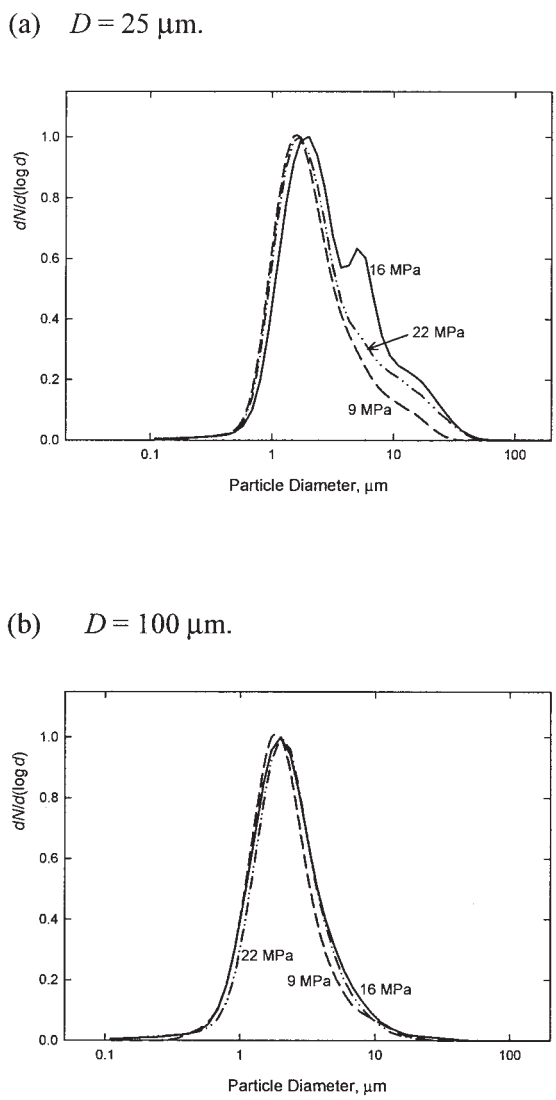

Figure 3. Experimental particle size distributions at T_0 = 353 K and different preexpansion pressures for nozzles with: (a) D = 25 μm; (b) D = 100 μm.

mainly relatively small spheres. This conclusion is also supported by the SEM microphotographs shown in a previous work[1] at T_0 = 359 K.

RESS results

To investigate the role of the RESS mechanism in the PGSS process, we carried out some specific RESS experiments using two different nozzle orifices (D = 25 μm and D = 100 μm) at P_0 = 16 MPa to verify the particle morphology and particle size.

Figures 5a and 5b show SEM microphotographs for particles produced by the RESS process. With support on the SEM images and counting more than 400 particles, we used SigmaScan software to obtain the mean diameter of the very small particles produced by RESS. This procedure was adopted because the particles obtained by RESS have sizes below the detection limit of the Aerosizer apparatus. Results showed that particles produced from the RESS process are mostly about 0.3

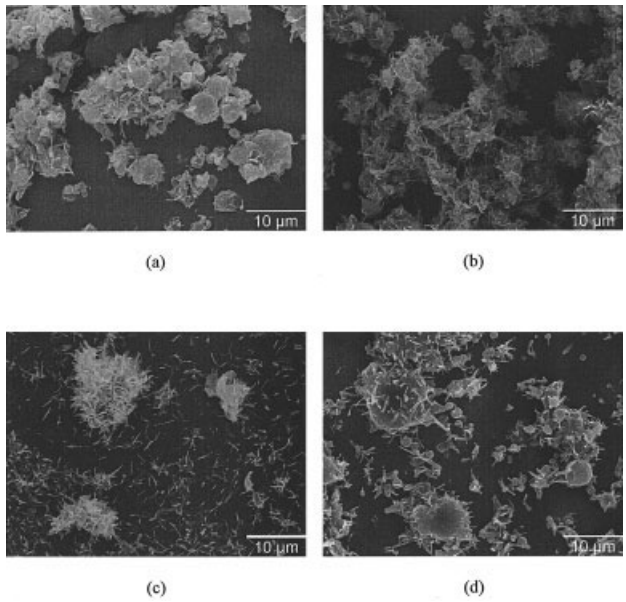

Figure 4. SEM microphotographs at different operating conditions (nozzle with D = 100 μm).

(a) T_0 = 353 K, P_0 = 9 MPa; (b) T_0 = 353 K, P_0 = 22 MPa; (c) T_0 = 333 K, P_0 = 16 MPa; (d) T_0 = 373 K, P_0 = 16 MPa.

μm in size for the D = 25 μm nozzle, about 10 times smaller than the particles obtained from PGSS, and 0.9 μm for the D = 100 μm nozzle, about two times smaller than the particles obtained from PGSS.

From Figure 5 and the particle size analysis we conclude that particles produced by RESS are irregular in shape and very small. Also, their morphologies are different from those produced by PGSS at similar operating conditions (compare Figure 4c to Figure 5b).

We emphasize that, because of the large fluid flow rate involved with the 100-μm nozzle, it is difficult to control and maintain the preexpansion conditions that may affect the expected results, in particular the size of the particles.

Mathematical Modeling

Hydrodynamics

Figure 6 shows a schematic representation of the PGSS process through a capillary nozzle, described as an annular-mist flow pattern. There can be different flow patterns, such as

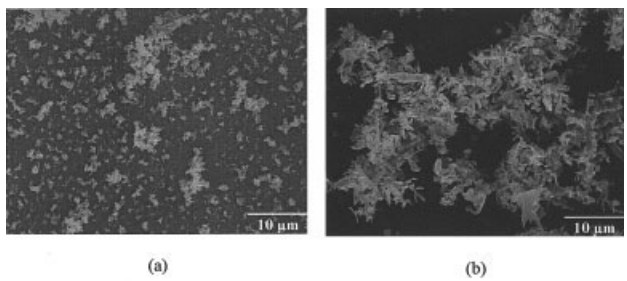

Figure 5. Typical SEM microphotographs of particles obtained by RESS at P_0 = 16 MPa.

(a) D = 25 μm, T_0 = 353 K; (b) D = 100 μm, T_0 = 333 K.

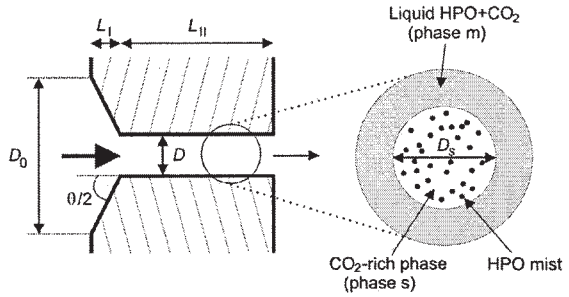

Figure 6. Typical nozzle and an annular-mist flow pattern in a PGSS process.

stratified, annular, intermittent, and bubble flows, for a two-phase gas–liquid flowing simultaneously in a pipe. In the region of high gas and liquid velocities, a dispersed bubble flow or an annular-mist flow may exit; the latter usually occurs at very high gas velocity. In this pattern, HPO mixes with CO_2 to form a CO_2-rich phase (phase s); around this phase, a liquid HPO (phase m) is in contact with the nozzle wall and is saturated in CO_2. The CO_2-rich phase also contains some HPO entrained by CO_2 because of its high speed; strictly, it includes two parts: entrained HPO and CO_2 saturated in HPO. We assume the CO_2-rich phase as a pseudophase (phase s).

The nozzle device consists of a converging inlet with diameter D_0, length L_I, and apex angle θ, followed by a straight capillary with diameter D and length L_{II}. The flow of the HPO/CO_2 mixture in the device is assumed as one-dimensional and inviscid because the liquid HPO-rich phase is highly expanded as a result of the large amount of CO_2 dissolved inside the nozzle.[2] Generally, temperatures (T_s and T_m), velocities (u_s and u_m), molar enthalpies (h_s and h_m), and densities (ρ_s and ρ_m) of the two phases are different, whereas the system pressure P is the same, as required by the mechanical equilibrium condition.

Then, the governing equations including mass, momentum, and energy conservations for a steady-state PGSS process can be written as

$$\frac{d(\rho_s M_s u_s A_s)}{dz} + \frac{d(\rho_m M_m u_m A_m)}{dz} = 0 \quad (1)$$

$$\frac{d(\rho_s M_s u_s u_s A_s)}{dz} + \frac{A_s dP}{dz} + \tau_{sm}\Omega_{sm} - \rho_s M_s g A_s + \Omega_{sm} u_{sm}\left(\varepsilon_0 + \frac{m_{sm}}{2}\right) = 0 \quad (2)$$

$$\frac{d[\rho_s M_s u_s (h_s/M_s + u_s^2/2) A_s]}{dz} + \frac{d(q_{sm})}{dz} + \frac{d(q_L)}{dz} + \frac{d(q_{mt})}{dz} - \rho_s M_s u_s g A_s = 0 \quad (3)$$

$$\frac{d[\rho_m M_m u_m A_m (1 - w_1)]}{dz} + \frac{d(m_1 \rho_2 M_2 u_s A_s)}{dz} = 0 \quad (4)$$

$$\frac{d(\rho_m M_m u_m u_m A_m)}{dz} + \frac{A_m dP}{dz} + \tau_{wm}\Omega_m - \tau_{sm}\Omega_{sm} - \rho_m M_m g A_m - \Omega_{sm} u_{sm}\left(\varepsilon_0 - \frac{m_{sm}}{2}\right) = 0 \quad (5)$$

$$\frac{d[\rho_m M_m u_m (h_m/M_m + u_m^2/2) A_m]}{dz} + \frac{d(q_{wm})}{dz} - \frac{d(q_{sm})}{dz} - \frac{d(q_L)}{dz} - \frac{d(q_{mt})}{dz} - \rho_m M_m u_m g A_m = 0 \quad (6)$$

Equations 1–3 are, respectively, the mass conservation equation for the total fluid, the momentum conservation equation, and the energy conservation equation in phase s. Although this pseudophase s has been treated before as a homogeneous model,[2] it would bring undesired complications for the annular-mist flow mode assumed here. Therefore, we consider independently the pure CO_2 and the entrained crystallized HPO (mechanically entrained HPO is neglected) because HPO is sparingly soluble in CO_2 and can be neglected in the hydrodynamic equations above. Then, for the mass balance we have

$$\rho_s M_s u_s A_s = \rho_1 M_1 (1 - m_1) u_s A_s + \rho_2 M_2 m_1 u_s A_s \quad (7)$$

Here, the first moment m_1 represents the solid (or particle) volume per unit volume of fluid from the melt crystallization (see Eq. 9). ρ_1 and M_1 are, respectively, the molar density and the molar mass of pure CO_2; ρ_2 and M_2 are, respectively, the molar density and the molar mass of HPO.

Equations 4–6 are, respectively, the HPO mass conservation equation, the momentum conservation equation, and the energy conservation equation in phase m.

In the governing equations, M_s and M_m are the average molar masses of the components in phase s and in phase m, respectively; w_1 is the mass fraction of CO_2 in phase m. In addition, Ω and A represent, respectively, the perimeter and the cross-sectional area of the nozzle. We will introduce later the friction forces between the nozzle wall and phase m (τ_{wm}) and between phase s and phase m (τ_{sm}), the heat-transfer rate from the nozzle wall (q_{wm}), the heat rate for the particle production by melt crystallization (q_L), and the heat transfer rate resulting from the mass transfer between two phases (q_{mt}). Equations 2, 3, 5, and 6 include the gravity effect for a vertically placed nozzle.

Crystallization

Melt Crystallization by Supercooling. In phase s the melt crystallization of the HPO occurs whenever the phase temperature decreases to form supercooled HPO while it flows through the nozzle. As discussed before[2] by considering particle condensation, coagulation, and nucleation, for one-dimensional flow the general dynamic equation is

$$\frac{\partial m_k}{\partial t} = -\frac{\partial(u_s m_k A_s)}{A_s \partial z} + G v^{-2/3} k m_{k-1/3} + J(v^*)(v^*)^k + (\dot{m}_k)_{coag} \quad (8)$$

where m_k is the kth moment given by

$$m_k = \int_0^\infty v^k n(v) \mathrm{d}v \tag{9}$$

where n denotes the particle size distribution function based on the particle volume v and v^* is the critical nucleus volume estimated from

$$v^* = \frac{32\pi}{3} \chi v_2 \left(\frac{T}{T_{\mathrm{fus}} - T} \right)^3 \tag{10}$$

In Eq. 8, G is the nucleus volume growth rate and J is the nucleation rate. The last term of Eq. 8 represents the moment change arising from particle coagulation, which can be neglected because of the short residence time of particles in the nozzle. The molecule's volume v_2 is estimated from $v_2 = 1/(\rho_2 N_{\mathrm{A}})$, where N_{A} is Avogadro's constant.

In Eq. 10, factor χ is close to unity and the difference ($T_{\mathrm{fus}} - T$) is the supercooling. For Eq. 9, a log-normal function is selected for the volume-based particle size distribution function

$$n(v) = \frac{m_0}{\sqrt{2\pi}(3 \ln \sigma_{\mathrm{g}}) v} \exp\left[- \frac{\ln^2(v/v_{\mathrm{g}})}{2(3 \ln \sigma_{\mathrm{g}})^2} \right] \tag{11}$$

The relations between the geometric average particle volume v_{g} and the geometric standard deviation σ_{g} with the moments are easily deduced.[2] According to Eq. 11, a diameter-based particle size distribution function can be written as

$$p_{\mathrm{C}}(d) = \frac{dN}{d \ln d} = \frac{1}{\sqrt{2\pi}(\ln \sigma_{\mathrm{g}})} \exp\left[- \frac{\ln^2(d/d_{\mathrm{g}})}{2(\ln \sigma_{\mathrm{g}})^2} \right] \tag{12}$$

where N is the particle density that has been nondimensionlized, that is, divided by m_0. The average particle diameter on a number basis is calculated from

$$d_{\mathrm{C}} = \frac{m_{1/3}}{m_0} \tag{13}$$

where $m_{1/3}$ is a fractional moment obtained from Eq. 9 with $k = 1/3$.

As discussed before,[2] the nucleation rate for the melt crystallization is given by

$$J = J_0 \exp\left[- \frac{k_j}{(T - T_{\mathrm{fus}})^2 T} \right] \tag{14}$$

In this equation, the preexponential factor J_0 is taken[4] as 10^{39} particles $\mathrm{m}^{-3}\ \mathrm{s}^{-1}$, k_j is a correlating parameter, and T_{fus} is the melting temperature of HPO. By assuming a three-dimensional growth, the nucleus diameter growth rate is

$$G = 3 \left(\frac{\pi}{6} \right)^{1/3} v^{2/3} G_0 \exp\left[- k_{\mathrm{g}} \frac{T_{\mathrm{fus}}^2}{(T_{\mathrm{fus}} - T)^2 T} \right] \tag{15}$$

In Eq. 15, G_0 and k_{g} are correlating parameters.

Solution Crystallization by Supersaturation. HPO crystallization occurs when the drastic drop in phase temperature and pressure causes a HPO supersaturation state in the CO_2-rich phase; this is a typical RESS process. Considering particle condensation, coagulation, and nucleation, the particle balance equation is the same as Eq. 8 for one-dimension flow. However, the critical nucleus volume should now be estimated from

$$v^* = \frac{32\pi}{3} \left(\frac{\sigma v_2^{2/3}}{kT} \right)^3 \left[\frac{1}{\ln S - K y_2^e (S - 1)} \right]^3 \tag{16}$$

In Eq. 16 σ, the interfacial tension between CO_2 and solid HPO, is assumed[5-7] to be 0.02 N m^{-1}. In addition, k is Boltzmann's constant, S is the supersaturation, and y_2^e is the solute's saturated mole fraction in pure CO_2. Parameter K is assumed to be zero when the supersaturation is expressed as $S = \phi(T, P, y_2) y_2 / \phi(T, P, y_2^e) y_2^e$, where y_2, the molar fraction of the solute in CO_2, is conveniently replaced by the equilibrium solute molar fraction at the nozzle entrance, and ϕ is the solute fugacity; this last equation was used by Helfgen et al.[6] in their modeling of the RESS process.

The nucleation rate J and an average particle volume growth rate G between the continuum regime to the free molecule regime are, respectively, expressed by[5]

$$J = 2 N_{\mathrm{A}} \frac{P y_2}{\sqrt{2\pi k T_s M_2 / N_{\mathrm{A}}}} \left(\frac{\sigma v_2^2}{kT} \right)^{1/2} \times \exp\left\{ - \frac{16\pi}{3} \left(\frac{\sigma v_2^{2/3}}{kT} \right)^3 \left[\frac{1}{\ln S - K y_2^e (S - 1)} \right]^2 \right\} \tag{17}$$

$$G = 2\pi d_{\mathrm{R}} D_e (y_2 - y_2^e) \rho_1 N_{\mathrm{A}} v_2 \left(\frac{1 + \mathrm{Kn}}{1 + 1.71\ \mathrm{Kn} + 1.333\ \mathrm{Kn}^2} \right) \tag{18}$$

In the equations above, D_e is the diffusion coefficient of the solute molecule in the fluid phase and Kn is the Knudsen number; they can be estimated using the formulae shown in the appendix of Kwauk and Debenedetti's work.[5] In Eq. 18, the driving force ($y_2 - y_2^e$) for particle growth was simplified here by assuming flat surfaces for the particles; d_{R} is the average particle size from the RESS process, calculated from Eq. 13. In addition, $p_{\mathrm{R}}(d)$, the diameter-based particle size distribution is given by Eq. 12 with the geometric average particle volume v_{g} and the geometric standard deviation σ_{g} obtained by solving Eqs. 8, 9, and 16–18.

Atomization

Previous work[2] showed that the temperature of phase m changes very little and that the relative velocities of the two phases (m and s) change along the nozzle, with their differences becoming larger along the flow direction. This means that the melt crystallization plays only a negligible role in the liquid HPO-rich phase m and that atomization should instead be considered as the mechanism of particle formation because of the interaction between the two phases.

Atomization processes, particularly for the air and burning

fuels such as diesel oil, have been widely studied. For the mean droplet diameter, the equation proposed by Nukiyama and Tanasawa[8] has been commonly used, although in most cases it shows a tendency to overestimate the droplet sizes. An alternative formula developed later by others, notably by Jasuja, well describe the mean droplet diameter d_A, written as[9]

$$d_A = 0.17\left(\frac{\sigma}{\rho_1}\right)^{0.45}\left(\frac{1}{u_{sm}}\right)^{0.9}\left(1+\frac{F_m}{F_s}\right)^{0.5} D^{0.55} + 0.015\left(\frac{\eta_m^2}{\sigma\rho_2}\right)^{0.5} \times \left(1+\frac{F_m}{F_s}\right) D^{0.5} \quad (19)$$

Here, σ is the interfacial tension of CO_2 and liquid HPO calculated from the data available for the supercritical CO_2/stearic acid system.[9] The relative velocity ($u_{sm} = u_s - u_m$) and the mass flow ratio of phase m to phase s (F_m/F_s) are obtained from the conservation equations. The viscosity of the mixed HPO/CO_2 phase (η_m) is estimated from the viscosity of CO_2 at the temperature and pressure of the mixture and from the viscosity of liquid HPO (see Eq. 38). The generalized Nukiyama–Tanasawa distribution,[8] adopted here to describe the droplet size spectra, is expressed as

$$p_A(d) = \frac{dN}{d\ln d} = \frac{(\zeta+1)d^{\xi+1}\exp\left(-\frac{d^\xi}{d_A/2}\right)}{\int_0^\infty\left[(\zeta+1)d^\xi\exp\left(-\frac{d^\xi}{d_A/2}\right)\right]dd} \quad (20)$$

where $\zeta = 2$ and $\xi = 1$ are commonly adopted. The mean diameter d_A is calculated from Eq. 19. Equations 19 and 20 indicate that, to obtain the droplet size and the size distribution, we need the relative velocity of the two phases and the density of phase m obtained from the hydrodynamic equations (Eqs. 1–6).

Variables in the model

The molar mass M_m of the liquid HPO-rich phase (HPO saturated with CO_2) is approximately obtained combining the molar fraction of CO_2 (x_1) with the molar masses of the pure components, CO_2 (M_1) and HPO (M_2). We assume that phase equilibrium exists between the CO_2 and the HPO in the liquid phase at preexpansion conditions. We chose the Peng–Robinson equation of state (PR-EOS) to calculate the phase equilibrium at preexpansion temperature and pressure conditions. The same equation of state is also used to describe the mixture's nonideality and the pure CO_2 properties. For the system pressure P, PR-EOS gives

$$P = \frac{RT\rho_i}{1-b\rho_i} - \frac{a\rho_i^2}{1+2b\rho_i-b^2\rho_i^2} \quad (21)$$

with the mixing rules

$$a = \sum_i\sum_j x_i x_j (a_i a_j)^{1/2}(1-k_{ij}) \quad (22)$$

$$b = \sum_i\sum_j x_i x_j\left(\frac{b_i+b_j}{2}\right) \quad (23)$$

In Eq. 21 subscript i denotes each phase: $i = 1$ for phase s (assumed pure CO_2) and $i =$ m for the liquid HPO-rich phase; on the contrary, i or j in Eqs. 22 and 23 represent either pure CO_2 or pure HPO.

According to mechanical equilibrium condition and Eq. 21

$$\frac{dP}{dz} = \left(\frac{\partial P}{\partial T_s}\right)_{\rho_1}\frac{dT_s}{dz} + \left(\frac{\partial P}{\partial \rho_1}\right)_{T_s}\frac{d\rho_1}{dz} = \left(\frac{\partial P}{\partial T_m}\right)_{\rho_m}\frac{dT_m}{dz} + \left(\frac{\partial P}{\partial \rho_m}\right)_{T_m}\frac{d\rho_m}{dz} \quad (24)$$

The derivatives of the molar enthalpies to the length coordinate can be expressed as

$$\frac{dh_i}{dz} = \left(\frac{\partial h_i}{\partial T_i}\right)_{\rho_i}\frac{dT_i}{dz} + \left(\frac{\partial h_i}{\partial \rho_i}\right)_{T_i}\frac{d\rho_i}{dz} \quad (25)$$

The partial derivatives of the molar enthalpies of each phase in Eq. 25 and the partial derivatives of total pressure to temperature and density in Eq. 24 can be obtained from the PR-EOS. For the molar enthalpy, the PR-EOS gives

$$h_i = h_i^{id} + RT(Z_i-1) - \frac{1}{2\sqrt{2}b}\left[a - T\frac{da}{dT}\right]\ln\frac{1+(\sqrt{2}+1)\rho_i}{1-(\sqrt{2}-1)\rho_i} \quad (26)$$

where, as before, $i = 1$ for phase s and $i =$ m for the liquid HPO-rich phase. The ideal-gas enthalpy for pure CO_2 is easily obtained[10]; the ideal-gas state enthalpy for the mixed phase, a composition average of the CO_2 and HPO enthalpies, is expressed as

$$h_m^{id} = x_1 h_1^{id} + (1-x_1)h_2 \quad (27)$$

with the enthalpy for pure HPO obtained from

$$h_2 = \int_0^{T_{fus}} C_{P2,sol}\,dT + \Delta_{fus}H + \int_{T_{fus}}^{T} C_{P2,liq}\,dT \quad (28)$$

where $\Delta_{fus}H$ is the fusion enthalpy of HPO and subscripts sol and liq denote, respectively, the solid and the liquid states. Also, we assume in Eq. 28 a reference state for HPO, whereas the enthalpy is zero for a perfect crystal at $T = 0$ K. Similarly, the enthalpy of the CO_2-rich phase is given by

$$h_s = \frac{\rho_1(1-m_1)}{\rho_s}h_1 + \frac{\rho_2 m_1}{\rho_s}h_2 \quad (29)$$

In Eqs. 2 and 5 τ_{sm} and τ_{wm} represent the friction forces produced separately by phase s into phase m and by the nozzle wall into phase m; they can be represented by

$$\tau_{sm} = \frac{1}{2} f_{sm} \rho_1 M_1 u_{sm} |u_{sm}| \tag{30}$$

$$\tau_{wm} = \frac{1}{2} f_m \rho_m M_m u_m^2 \tag{31}$$

where f_{sm} and f_m are the Fanning friction factors corresponding to different contact interphases. Typically, the value of 0.0125 for both coefficients is adopted for a plain-orifice–type nozzle. Also, the last terms on the left-hand sides in Eqs. 2 and 5 are the momentums from phase change and the Reynolds flux where one-half of the forces thus produced is approximately ascribed to each phase (s and m). According to Wallis,[8] ε_0 is the irreversible Reynolds flux per unit area of the interface (which is neglected), and m_{sm} is the rate of vaporization (only CO_2 is considered here) per unit area of the interface, expressed as

$$m_{sm} = -\frac{1}{\Omega_{sm}} \frac{d(\rho_m M_m u_m A_m w_1)}{dz} \tag{32}$$

In Eq. 3 the heat flux term (q_L), produced when the temperature drops below the HPO fusion temperature, is expressed as a function of the first moment m_1

$$\frac{dq_L}{dz} = -\Delta_{fus} H \frac{d(m_1 \rho_2 u_s A_s)}{dz} \tag{33}$$

In Eq. 6 the heat-transfer term through the nozzle wall (q_{wm}) and the heat-exchange term between the two phases (q_{sm}) are, respectively, given by

$$\frac{dq_{wm}}{dz} = -\alpha_w (T_w - T_m)\Omega \tag{34}$$

$$\frac{dq_{sm}}{dz} = -\alpha_{sm} (T_m - T_s)\Omega_{sm} \tag{35}$$

The minus sign in Eqs. 34 and 35 represents heat flow from the wall to the fluid and from phase m to phase s; T_w is the wall temperature and Ω and Ω_{sm} are, respectively, the perimeters of the nozzle and of the core phase (phase s). The transfer coefficients of heat convection from the nozzle wall to phase m (α_w) and from phase m to phase s (α_{sm}) are given by

$$\alpha_w = 0.023 \frac{\lambda_m}{D} \mathrm{Re}^{0.8} \mathrm{Pr}^c \tag{36}$$

$$\alpha_{sm} = 0.023 \frac{\lambda_1}{D_s} \mathrm{Re}^{0.8} \mathrm{Pr}^c \tag{37}$$

where c is 0.3 for cooling and 0.4 for heating.

The velocity term in the expression for Re in Eq. 36 is u_s, whereas that for Re in Eq. 37 is the relative velocity; D_s is the diameter of the core phase s. The viscosity of pure CO_2 at high pressures and different temperatures is calculated from data available elsewhere.[9] For the CO_2/HPO mixture, however, the viscosity is calculated from an empirical expression using pure CO_2 and pure HPO viscosity data

$$\ln(\eta_m/\rho_m) = x_1 \ln(\eta_1/\rho_1) + (1 - x_1)\ln(\eta_2/\rho_2) \tag{38}$$

The thermal conductivity of pure CO_2 is correlated using data of Michels et al.[11] For the CO_2/HPO mixture it is approximately calculated from

$$\lambda_m = w_1 \lambda_1 + (1 - w_1)\lambda_2 - 0.72 w_1 (1 - w_1)(\lambda_2 - \lambda_1) \tag{39}$$

In Eq. 39, the thermal conductivity of pure HPO (λ_2) is taken roughly as 0.15 W/mK and the effect of temperature is neglected.

The heat capacities are calculated from the PR-EOS for each phase

$$C_{Vi} = C_{Vi}^{id} + \frac{T_i}{2\sqrt{2}b} \left(\frac{d^2 a}{dT_i^2} \right) \ln \left[\frac{1 + (1 + \sqrt{2})b\rho_i}{1 + (1 - \sqrt{2})b\rho_i} \right] \tag{40}$$

$$C_{Pi} = C_{Vi} + \frac{R[Z_i + T_i(\partial Z_i/\partial T_i)_{\rho_i}]}{Z_i + \rho_i(\partial Z_i/\partial \rho_i)_{T_i}} \tag{41}$$

As before, $i = 1$ for pure CO_2, and $i = m$ for the liquid HPO-rich phase.

In Eqs. 3 and 6 the heat-transfer term (q_{mt}) representing the mass transfer of CO_2 and HPO from phase m to phase s (it does not include the heat term given by Eq. 33) is calculated from

$$\frac{dq_{mt}}{dz} = -h_2 \frac{d(m_1 \rho_2 u_s A_s)}{dz} - \bar{h}_1 \frac{d(\rho_1 u_s A_s)}{dz} \tag{42}$$

where $\bar{h}_1$ is the average enthalpy for CO_2 between $z - dz$ and z, that can be approximately assigned to be $h_1(z)$.

Finally, it is convenient to introduce a new parameter, β, defined as the cross-sectional area fraction of the CO_2-rich phase, related to the cross-sectional areas A_s and A_m in Eqs. 1–6 by

$$A_s = \beta A \qquad A_m = (1 - \beta) A \tag{43}$$

Numerical Solution

Solving simplifications

To obtain particle characterization we need the three moments ($k = 0$, 1, and 2) of Eq. 9 with $dm_i/dt = 0$ at steady-state conditions. Equation 9 is used for the melt crystallization and for the RESS process, although they have to be calculated separately. Using the appropriate expressions for the variables presented above, the nine ordinary equations Eqs. 1–6 and Eq. 9 are numerically solved to give densities (ρ_1), temperatures (T_s and T_m), velocities (u_s and u_m), CO_2 mole fractions in phase m (x_1), and the first three moments (m_0, m_1, and m_2). The PR-EOS

then gives the total pressure (P) and the density of the mixed phase (ρ_m). In the nozzle-converging region, adiabatic and nonfrictional flow is commonly assumed and the irreversible Reynolds flux can usually be neglected.[8] We further assume:

(1) The CO_2/HPO mixture is replaced by the pseudobinary system CO_2/pure palm oil deodorizer condensate as described elsewhere,[12] where the HPO was represented by a stearic acid with its physical properties. This assumption is reasonable, considering only the most representative saturated fatty acids present in the HPO (which actually is a mixture of lipids).

(2) In Eqs. 14 and 15 we use the crystallization kinetic constants presented elsewhere.[2]

The Runge–Kutta–Fehlberg algorithm[13] is used to solve the ordinary differential equations with the initial guesses $m_i(0) = 0$ for the melt crystallization because no nucleation occurs before the HPO melting point. We adopt the conventional iteration technique for Mach number (Ma) equal to unity at chocked flow condition at the nozzle exit to search for the unknown preexpansion velocity. The (pseudo) Mach number is calculated from

$$\mathrm{Ma} = \sqrt{\frac{u_s^2}{[(C_{P1}/C_{V1})RT_s/M_1][Z_1 + \rho_1(\partial Z_1/\partial \rho_1)_{T_s}]}} \qquad (44)$$

However, at low preexpansion temperatures (such as 333 or 343 K) this iteration procedure cannot reach Ma = 1, as defined by Eq. 44. This is explained by the larger amounts of the solute that precipitate in the CO_2-rich phase, which deviates this phase from being a pure gas. For this reason, we use instead the iteration criterion[2] $d[z/(L_I + L_{II})]/d\mathrm{Ma} \leq 10^{-15}$.

At preexpansion temperature and pressure of 359 K and 18 MPa we obtain $\beta = 0.95$ by matching the calculated to the experimental CO_2 flow rate (~1.5 g/min) for the $D = 25$ μm nozzle. This value of β gives a calculated total solid production of about 110 mg/min that compares well to the experimental result (~100 mg/min). In addition, $\beta = 0.95$ also agrees with the experimental CO_2 flow rate (~30 g/min) and the total solid production (an average of 2.1 g/min in all runs) for preexpansion temperatures in the range 333–353 K, preexpansion pressure of 16 MPa, and for the nozzle with 100-μm diameter.

Using the assumptions above, Figures 7–9 give the calculated results for the nozzle dimensions and other conditions listed in Table 1.

Calculated results

Variables from Hydrodynamic Equations. Figures 7–9 give the profiles along the nozzle for the total pressure, Mach number, CO_2 mole fraction in the HPO-rich liquid phase, and for the densities, velocities, and temperatures of the two phases (phase s and phase m). As Figure 7 shows, in this annular-mist flow pattern the profiles for total pressure, temperature, and density of the CO_2-rich phase are similar to those obtained for the dispersed bubble flow pattern.[2] The dotted lines in Figure 7 represent the profiles of the same variables after the nozzle up to the Mach disk—the jet-free process. (We assumed that the temperature of this part is 293 K and that the flow is pure CO_2 only.) Figure 8 indicates that the density of the liquid HPO phase decreases slightly when the flow moves from the converging region into the straight capillary, although the calculations show that there is a sharp increase at the nozzle exit because of the corresponding decrease in temperature. The CO_2 mole fraction in liquid HPO shows a similar trend after the change of the density of the liquid HPO phase. The temperature of phase m decreases slowly in the nozzle but rapidly at the nozzle's exit. The temperature profile indicates that the HPO in phase m is melted before the nozzle's exit. Figure 9 indicates that there is a substantial difference in the velocities of the two phases in the nozzle.

Although there are a number of variables that affect the simulation results of the hydrodynamic equations, we note that

Table 1. Simulation Conditions Used in the Calculations*

D (μm)	D_0 (μm)	L_I (μm)	L_{II} (μm)	T_w (K)
25 or 100	300 or 1200	100	250	$=T_0$

*Values of k_{ij}, f, k_g, k_j, J_0, G_0, and HPO fusion data (T_{fus}, $\Delta_{fus}H$) were taken from Li et al.[2]

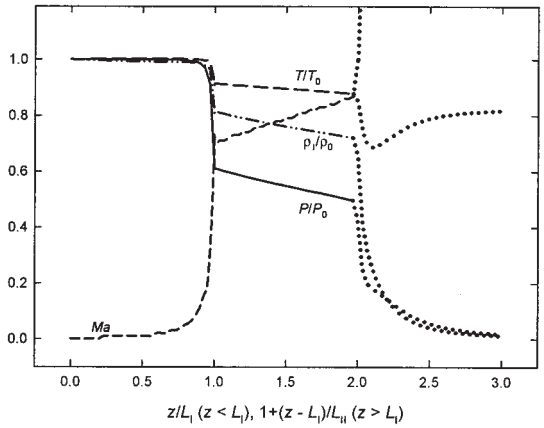

Figure 7. Pressure, density, temperature, and Mach number profiles in the nozzle and after the nozzle (dotted lines) for the supercritical phase.

$P_0 = 16$ MPa, $T_0 = 353$ K, $D = 100$ μm.

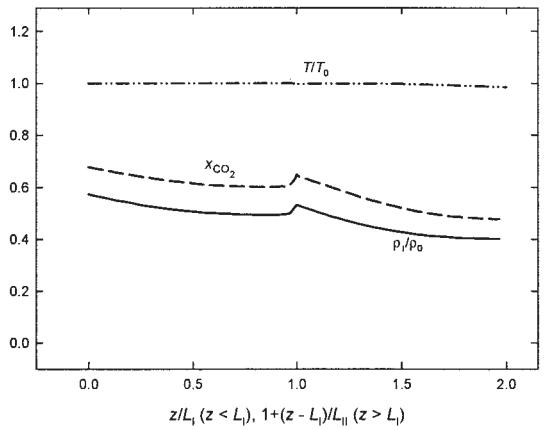

Figure 8. Temperature, CO_2 mole fraction and density profiles in the nozzle for the liquid HPO-rich phase.

$P_0 = 16$ MPa, $T_0 = 353$ K, $D = 100$ μm.

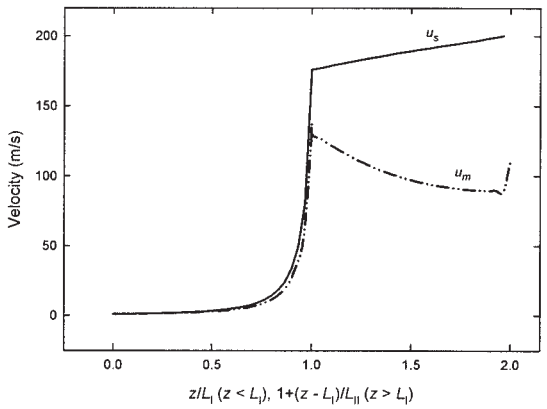

Figure 9. Velocity profiles of the two phases along the nozzle.

P_0 = 16 MPa, T_0 = 353 K, D = 100 μm.

the heat-transfer term q_{sm} of the forced convection between the two phases plays an important role. With the increase of these heat-transfer coefficients, the Mach number easily reaches unity and it changes the profiles shown in Figures 7–9, notably the temperature of phase m at the nozzle's capillary zone.

Particle Size and Particle Production. Tables 2–6 show the calculated particle sizes and particle productions from different mechanisms under various operating conditions. In those tables, ψ_i represents the particle number fraction produced by atomization (i = A), by melt crystallization (i = C), and by RESS (i = R). Assuming that the particles are spheres, they were estimated from

$$\psi_i = (F_i/d_i^3)/(F_A/d_A^3 + F_C/d_C^3 + F_R/d_R^3) \qquad (i = A, C, R) \quad (45)$$

In Eq. 45, F_A, the mass flow rate of liquid HPO at the nozzle exit that is considered as the particle production through atomization (total HPO droplets can be transformed into solid particles after the nozzle), can be calculated from

$$F_A = [\rho_m u_m A_m (1 - x_1) M_2]_{\text{nozzle exit}} \quad (46)$$

The particle production by the melt crystallization at the nozzle exit (F_C) is calculated from

$$F_C = (m_1 u_s A_s \rho_2 M_2)_{\text{nozzle exit}} \quad (47)$$

The particle production by RESS at the nozzle exit (F_R) is calculated as

Table 2. Calculated Particle Size and Produced Particle Yield at Different Preexpansion Pressures*

P_0 (MPa)	d_A	d_C	d_R	F_A	F_C	F_R	ψ_A
9	217	47	0.94	78	21	0.002	0.04
16	108	47	3.4	96	15	0.97	0.34
22	69	68	48	111	8.7	13	0.92 (0.70**)

*T_0 = 353 K, D = 25 μm; d_i in nm, F_i in mg/min.
**Includes RESS contribution.

Table 3. Calculated Particle Size and Produced Particle Yield under Different Preexpansion Temperatures*

T_0 (K)	d_A	d_C	d_R	F_A	F_C	F_R	ψ_A
333	276	57	36	96	143	7.7	0.006 (0.005**)
343	108	54	28	96	31	2.5	0.28 (0.20**)
353	108	47	3.4	96	15	0.97	0.34
359	112	55	3.7	96	7.2	0.65	0.62
363	114	62	2.8	97	3.5	0.53	0.81

*P_0 = 16 MPa, D = 25 μm; d_i in nm, F_i in mg/min.
**Includes RESS contribution.

$$F_R = (\rho_s u_s A_s y_2^e M_2)_{\text{nozzle entrance}} \quad (48)$$

Equation 48 assumes that saturated HPO in supercritical CO_2 at the nozzle entrance can be totally precipitated. It is therefore a maximum estimation, considering that the RESS process continues after the nozzle.

As Tables 2–6 show, for the 25-μm nozzle the particle size dependency is similar to that found in previous studies for the melt crystallization and the atomization processes. For the supersaturation crystallization (RESS) process, the particle size depends weakly on the preexpansion conditions, except for low temperatures and high pressures, and is about 10 to 50 times smaller than that from the melt crystallization process and about 10 to 500 times smaller than that from the atomization process. The particles produced from the atomization process have the largest sizes under the conditions studied here. Comparing the particle production from the different mechanisms, as given by F_A, F_C, and F_R in Tables 2–6, the atomization process has the highest HPO mass conversion into particles; the second highest particle production is usually the melt crystallization. The results shown in Tables 2–6 also indicate, however, that particle production from RESS should not be neglected at high preexpansion pressures or at low preexpansion temperatures; also, the particle production from the melt crystallization is comparatively as high as that from the atomization process at low preexpansion temperatures. Because the size of particles formed by the RESS process is very small, the number percentile of those particles is high, although the total mass of particles is very low. The ψ_A values presented in Tables 2–6 were in most cases calculated by neglecting the particles produced from the RESS process (except for the cases denoted by asterisks); this is because our RESS experiments confirmed that most particles had a mean diameter of about 0.3 μm and thus were not clearly shown in the measured particle size distribution curves obtained with the Aerosizer. The comparison of the ψ_A values in those tables reveals that the populations of particles produced by melt crystallization are larger than those obtained by atomization for the D = 100 μm nozzle, except for the cases at high preexpansion pressures or at high preexpan-

Table 4. Calculated Particle Size and Produced Particle Yield under Different Preexpansion Pressures*

P_0 (MPa)	d_A	d_C	d_R	F_A	F_C	F_R	ψ_A
9	498	50	1.1	1389	175	0.01	0.008
16	224	56	5.0	1685	177	8.5	0.13
22	151	68	47	1928	141	134	0.55 (0.56**)

*T_0 = 353 K, D = 100 μm; d_i in nm, F_i in mg/min.
**Includes RESS contribution.

Table 5. Calculated Particle Size and Produced Particle Yield under Different Preexpansion Temperatures*

T_0 (K)	d_A	d_C	d_R	F_A	F_C	F_R	ψ_A
333	213	66	36	1636	541	103	0.08 (0.04**)
343	210	61	27	1665	395	27	0.11 (0.06**)
353	224	56	5.0	1685	177	8.5	0.13
363	243	67	3.2	1702	37	4.1	0.49
373	273	0.46	3.2	1712	0	3.0	1

*P_0 = 16 MPa, D = 100 μm; d_i in nm, F_i in mg/min.
**Includes RESS contribution.

sion temperatures; on the contrary, they are approximately comparable for the D = 25 μm nozzle.

Particle Size Distribution. The combined particle size distribution for particles obtained from the three mechanisms can be described as

$$p(d) = \sum \psi_i p_i(d) \qquad (i = \text{A, C, R}) \tag{49}$$

Figures 10 and 11 illustrate the calculated particle size distributions under different operating conditions. For most cases studied here we consider only two spectra from the melt crystallization and from the atomization at the nozzle exit for the same reason as mentioned above. In the same figures, the normalization is performed to give a clear comparison with the experimental particle size distributions. Figure 10 shows that the particle spectrum changes with preexpansion temperatures and nozzle dimensions. As Tables 3 and 5 show, ψ_A and the difference between d_A and d_C apparently change with increasing preexpansion temperature. For the D = 25 μm nozzle, because the atomization and the melt crystallization are comparable, it produces mainly bimodal particle distributions. For the D = 100 μm nozzle, usually only unimodal particle spectra can be found for the cases studied here because the melt crystallization always prevails over the atomization. In cases where the atomization becomes suddenly predominant, however, we also obtain unimodal spectra. Figure 11 shows that the particle spectrum changes drastically with the preexpansion pressure, passing from unimodal to bimodal distributions. This is explained by the variations of ψ_A, d_A, and d_C in Tables 2, 4, and 6 for the same reasons as mentioned above. Again, for the D = 100 μm nozzle there is no evident bimodal particle spectrum for the studied preexpansion pressures.

Impact of some variables on particle formation

We previously reported[14] that the temperature–pressure melting behavior significantly affects the simulated particle information. For example, using a pressure-independent melting temperature, the particle size distribution from the melt crystallization widens and the particle number increases when compared with similar results assuming a pressure-dependent melting temperature along the nozzle. Therefore, the melting temperature that appears in Eqs. 14, 15, and 28 is assumed to be pressure dependent.[14] This means that different solutes may give quite different particle information depending on their melting pressure–temperature behaviors.

Table 6. Calculated Particle Size and Produced Particle Yield under Different Preexpansion Pressures*

P_0 (MPa)	d_A	d_C	d_R	F_A	F_C	F_R	ψ_A
12	167	54	1.4	87	73	0.03	0.28
14	133	54	2.1	91	7.7	0.16	0.44
16	111	55	3.7	96	7.2	0.65	0.62
18	95	56	5.8	102	6.8	2.0	0.76

*T_0 = 359 K, D = 25 μm; d_i in nm, F_i in mg/min.

(a) D = 25 μm.

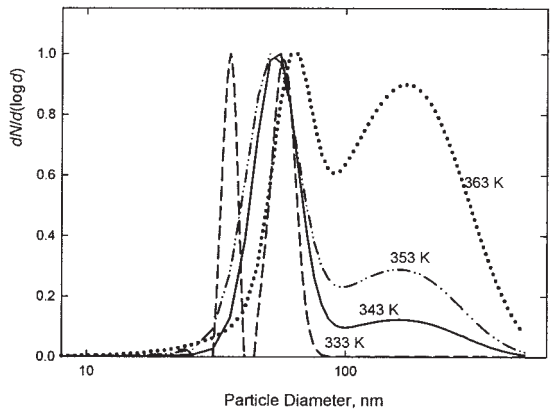

(b) D = 100 μm.

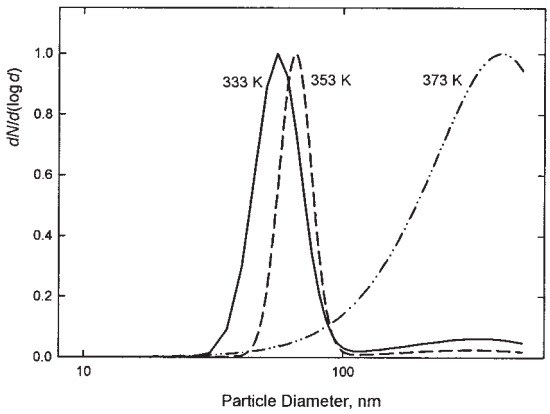

Figure 10. Effect of the preexpansion temperature on the particle size distribution at P_0 = 16 MPa.
(a) D = 25 μm; (b) D = 100 μm.

Parameter ξ in Eq. 20 has an obvious influence on the distribution of particles from the atomization process. Figure 12a shows the calculated particle size distributions at[8] ξ = 1 and ξ = 2. Figure 12a shows that increasing ξ narrows the particle size distributions from the atomization, thus changing the particle spectra. This comparison may also provide a choice for ξ, such that ξ = 2 is clearly preferable to ξ = 1 for the model system studied here. The crystallization kinetics constants k_g, G_0, and k_j affect the melt crystal formation. The influence of k_j on the particle spectra is evident from Figure 12b. This figure indicates that increasing k_j will accordingly increase the percentile of particles from the melt crystallization and dramatically change the calculated particle spectra from unimodal to bimodal; therefore, the accurate determination of this parameter is important. Although k_g and G_0 affect the calculated particle size, only for large values of G_0 (~0.1 m/s

for the system presented here) is their influence evident on the particle size because of the fluid's short residence time as discussed before.[2] Factor β reflects the flow-rate ratio of CO_2 over HPO; as emphasized above, it should be determined by the experimental CO_2 flow rate and the HPO particle output. Values of β may depend on the operating conditions, although

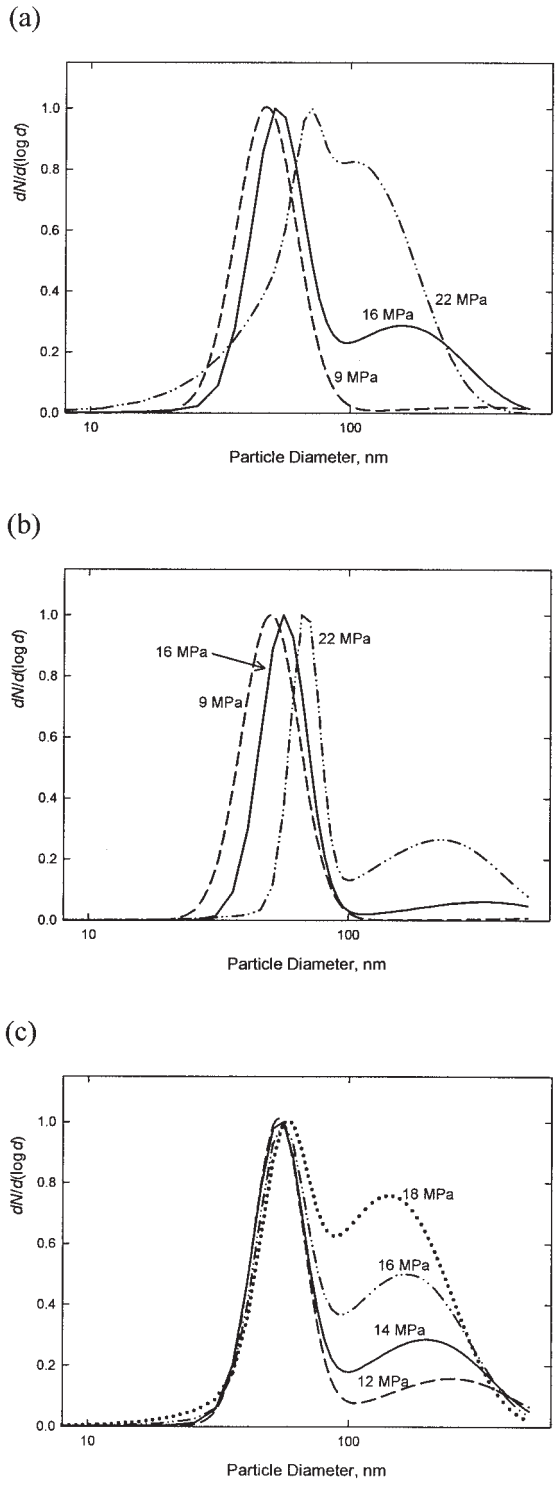

Figure 11. Effect of the preexpansion pressure on the particle size distribution at constant temperature.

(a) T_0 = 353 K, D = 25 μm; (b) T_0 = 353 K, D = 100 μm; (c) T_0 = 359 K, D = 25 μm.

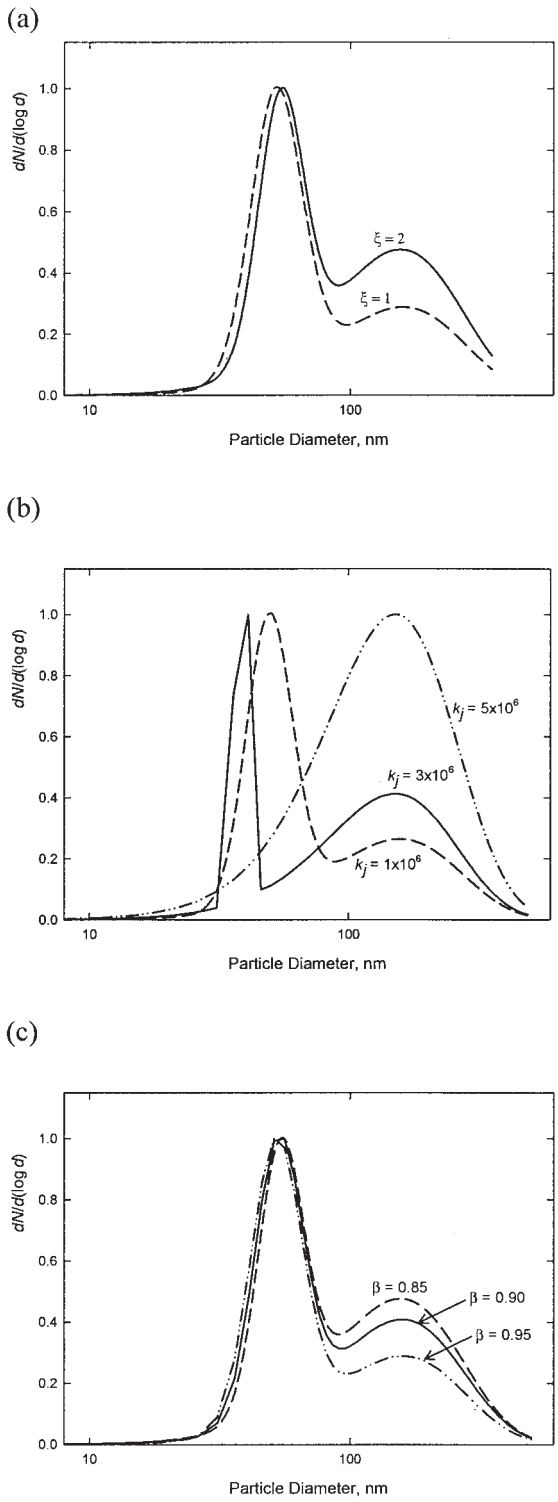

Figure 12. Effect of parameters ξ, k_j, and β on particle size distributions at P_0 = 16 MPa, T_0 = 353 K, and D = 25 μm.

(a) Parameter ξ; (b) parameter k_j; (c) parameter β.

Table 7. Experimental and Calculated Mean Particle Size at Constant Preexpansion Temperatures

Experiment (T_0 = 359 K, D = 25 μm)			Experiment (T_0 = 353 K, D = 25 μm)			Experiment (T_0 = 353 K, D = 100 μm)		
P_0 (MPa)	$\bar{d}$ (μm)	Calculated $\bar{d}$ (μm)	P_0 (MPa)	$\bar{d}$ (μm)	Calculated $\bar{d}$ (μm)	P_0 (MPa)	$\bar{d}$ (μm)	Calculated $\bar{d}$ (μm)
12	3.0	0.09	9	2.1	0.05	9	1.9	0.05
14	3.0	0.09	16	2.1	0.07	16	2.0	0.08
16	2.8	0.09	20	2.2	0.06	22	2.2	0.10

our studies did not indicate such a relationship because the dependency on the operation conditions from our experiments is not quite clear. The effect of β on particle size information is shown in Figure 12c: decreasing β clearly increases the percentile of particles from the atomization process and increases the particle size, which is in agreement with the findings of the homogeneous two-phase model presented elsewhere.[2]

Comparisons and Discussion

Particle size

Tables 7 and 8 list the calculated and the experimental mean particle sizes of HPO obtained from the PGSS process under different conditions. The mean particle size is calculated from

$$\bar{d} = \sum \psi_i d_i \qquad (i = \text{A, C, R}) \tag{50}$$

Similarly to Eq. 49 in most cases only two mechanisms (melt crystallization and atomization) are considered at the nozzle exit because the very small particles obtained from the RESS process could not be detected in our experiments. Results presented in Tables 7 and 8 indicate that most calculated particle sizes (at the nozzle exit) are about 30 times smaller than those obtained from experiment (although far from the nozzle exit). The trend of the calculated particle sizes with the operating conditions agrees with the experiment, although the calculated dependency on the operation conditions is slightly larger than the experimental dependency.

Particle size distributions

The experimental and calculated results shown in Figures 2 and 10 and in Figures 3, 11a, and 11b correspond to the same operating conditions. As shown, there is a reasonable (qualitative) agreement between the experimental and the calculated particle size distributions, notably for some typical bimodal distributions and for the unimodal distribution obtained with the D = 100 μm nozzle. At relatively high preexpansion temperatures, however, calculated particle size distributions show appreciable differences from the remaining cases, which indicates that the mechanism transition for the particle formation passes from a combining control of the melt crystallization and atomization to a pure atomization. The disagreement between the experimental and the predicted behaviors at high temperatures is likely explained by the fact that we collected only a few smaller particles in our experiments because other particles (that may have been produced by HPO droplet coagulation) were too large to be measured. The same disagreement may also obviously be ascribed to our theoretical model that does not consider the complex HPO coagulation in the after-nozzle part when the preexpansion temperature is high.

Table 8. Experimental and Calculated Particle Size at Constant Preexpansion Pressures

Experiment (P_0 = 16 MPa, D = 25 μm)			Experiment (P_0 = 16 MPa, D = 100 μm)		
T_0 (K)	$\bar{d}$ (μm)	Calculated $\bar{d}$ (μm)	T_0 (K)	$\bar{d}$ (μm)	Calculated $\bar{d}$ (μm)
333	1.8	0.06	333	2.6	0.06
343	2.1	0.06	343	—	0.05
353	2.1	0.07	353	2.0	0.08
363	2.5	0.1	373	2.2	0.3

Particle morphology

Combining the information above, especially the SEM microphotographs shown in Figures 4 and 5, the experimental and the calculated particle size distributions (shown in Figures 2, 3, 10, and 11), and the particle size information from different mechanisms (given by Tables 2–6), we conclude that different particle formation mechanisms produce different particle morphologies. At high preexpansion temperatures, Figure 4d shows that most of the particles are spheres; our calculated results (at T_0 = 363 K in Table 3 and at T_0 = 373 K in Table 5) show that atomization undoubtedly prevails over other mechanisms in this case. Therefore, the atomization process will produce spheres for the system presented here. At low preexpansion temperatures or low preexpansion pressures, Figure 4a or Figure 4c shows that there are some larger spheres and many crystals; our theoretical studies (T_0= 333 K in Table 5 and P_0 = 9 MPa in Table 2) show that melt crystallization prevails over other mechanisms in those cases. Therefore, the melt crystallization process will produce amorphous particles.

As mentioned in the experimental section, the RESS process produces small and amorphous crystals. Because we find only a few small crystals, we conclude that most of the RESS particles merge into the surfaces of the spheres obtained from atomization (they are liquid droplets when leaving the nozzle exit) when they pass through the after-nozzle zone. Therefore, we find many spheres full of crystals at their surfaces (such as those shown in Figures 4b and 4c), under conditions where there must exist many RESS-produced crystals, as indicated in Tables 4 and 5. The spheres have smoother surfaces (see Figures 4a and 4d) when the preexpansion pressure is relatively low or the preexpansion temperature is relatively high because there are very few RESS crystals produced under those conditions, as Tables 4 and 5 also indicate.

Conclusions

This work presents a general mathematical model of the PGSS process by assuming a one-dimensional, inviscid, and two-phase annular-mist flow. The crystallization and atomization mechanisms are both applied to account for particle formation in the PGSS process. The corresponding hydrodynamic equations and the general aerosol equation were established and solved numerically using realistic simplifications. Simulation provided information of temperature, total pressure, densities, velocities, CO_2 compositions, and particle size along the capillary nozzle, as well as different modes for particle size distributions. Comprehensive experimental results were used to compare with the theoretical studies.

Based on the experimental results we conclude:

(1) The PGSS process produces usually two kinds of particles: spheres and crystals with sizes of about 2–3 μm. The operating conditions with small nozzle diameters or high preexpansion temperatures or mild preexpansion pressures will tend to produce bimodal particle distribution curves.

(2) RESS-produced particles are amorphous and very small (particle size: $\sim$0.3 μm); they are much smaller than the crystals produced from the PGSS process. Most crystals shown in the SEM microphotographs are produced by PGSS.

Combing the experimental and the theoretical studies we further conclude:

(3) At the nozzle's exit, a narrow size distribution of small particles is obtained by melt crystallization, whereas a relatively wide size distribution of large particles is obtained by atomization.

(4) The atomization process produces (in mass) most of the HPO particles, fewer particles result from the melt crystallization process, and only a limited population of particles from the RESS process. For high preexpansion pressures, however, the particle production from the RESS process becomes comparable to that of the melt crystallization process, which cannot be neglected.

(5) In many cases the number percentage of particles produced by the melt crystallization process will prevail over that produced by the atomization process. Usually, only high preexpansion temperatures can produce particles mainly from atomization.

(6) PGSS-produced particles are expected to have unimodal to bimodal distributions, depending on the particle percentage following different particle formation mechanisms at different operating conditions.

(7) The atomization process produces spherical and relatively large particles; the melt crystallization process produces relatively large and amorphous particles; the small and amorphous particles produced by RESS may merge into the surfaces of the spherical particles and most of them may not exist independently. High preexpansion temperatures are favorable to the production of relatively small spheres with smooth surfaces.

(8) The nozzle diameter has only a negligible effect on the produced particle size, but has a more evident effect on the particle size distribution. Large nozzle diameters will usually produce unimodal distribution particles.

(9) The thermodynamic behavior of the pressure dependency of the melting temperature, the nucleation kinetic constants, the atomization model parameters, and the cross-sectional area fraction in the two-phase model are sensitive to the modeled particle information. They should be prudently determined before use.

(10) The dependency of the particle size on calculated operating conditions follows the experimental trend, although the calculated particle size (at the nozzle exit) is about 30 times smaller than the experimental size (far from the nozzle exit).

Acknowledgments

For financial support, the authors are grateful to FCT (Project POCTI/1999/EQU/34961 and post-doctoral grant BPD/5526/2001), to the European Union Programme FEDER, and to the NSFC China (Project 20406015).

Notation

A = cross-sectional area, m^2
a, b = parameters in PR-EOS
C_P = isobaric heat capacity, J K^{-1} mol^{-1}
C_V = isochoric heat capacity, J K^{-1} mol^{-1}
D = nozzle diameter, m
D_e = diffusion coefficient, m^2/s
d = particle diameter, m
f = Fanning friction factor
F = mass flow rate, g/s
g = gravity constant, m/s^2
G = nuclei volume growth rate, m^3/s
G_0 = correlating parameter, m/s
h = enthalpy, J/mol
$\Delta_{fus}H$ = enthalpy of fusion, J/mol
J = nucleation rate, particles m^{-3} s^{-1}
J_0 = correlating parameter, particles m^{-3} s^{-1}
K = parameter from Kwauk et al.[5]
k_g = correlating parameter, K^{-1}
k_j = correlating parameter, K^{-3}
k_{ij} = interaction parameter
Kn = Knudsen number
L = nozzle length, m
m_0 = zeroth moment, particles/m^3
m_1 = first moment, m^3/m^3
m_2 = second moment, m^3
M = molar mass, kg/mol
Ma = Mach number
N = particle density, particles/m^3
N_A = Avogadro's constant, molecules/mol
n = particle size distribution function, particles m^{-3} m^{-3}
p = normalized particle size distribution
P = pressure, MPa
Pr = Prandtl number
q = heat transfer rate, J/s
R = ideal gas constant, J K^{-1} mol^{-1}
Re = Reynolds number
S = supersaturation
T = temperature, K
T_{fus} = fusion temperature, K
u = axial velocity, m/s
v = particle volume, m^3
v_g = geometric average particle volume, m^3
x = mole fraction
w = mass fraction
Z = compressibility factor
z = nozzle length coordinate, m

Greek letters

α = convection heat transfer coefficient, W m^{-2} K^{-1}
β = cross-sectional area fraction of phase s
χ = form factor
ε_0 = irreversible Reynolds flux, g m^{-3} s^{-1}
ϕ = fugacity coefficient
η = viscosity, Pa·s

λ = thermal conductivity, W m^{-1} K^{-1}
θ = apex angle
ρ = molar density, mol/m^3
σ = interfacial tension, N/m
σ_g = geometric standard deviation
τ = friction shear stress, N/m^2
ψ = particle number fraction
ζ, ξ = parameters of atomization model
Ω = perimeter, m

Subscripts

0 = stagnation state
1 = CO_2
2 = HPO
A = atomization
C = melt crystallization
m = CO_2/HPO mixed liquid phase
L = heat transfer arising from enthalpy phase change
liq = liquid state
mt = heat transfer arising from mass transfer
R = RESS process
s = CO_2-rich phase
sm = between phase s and phase m
sol = solid state
w = wall
wm = between wall and phase m

Superscripts

$\bar{}$ = average value
id = ideal gas
e = equilibrium
* = critical

Literature Cited

1. Rodrigues M, Peiriço N, Matos HA, Gomes de Azevedo E, Lobato MR, Almeida AJ. Microcomposites theophylline/hydrogenated palm oil from a PGSS process for controlled drug delivery systems. *J Supercrit Fluids*. 2004;29:175-184.
2. Li J, Matos HA, Gomes de Azevedo E. Two-phase homogeneous model for particle formation from gas-saturated solution processes. *J Supercrit Fluids*. 2004;32:275-286.
3. Li J, Matos HA, Gomes de Azevedo E. Modeling of particle formation from a gas-saturated solution process. Proc of 6th Int Symp on Supercritical Fluids, Versailles, France; 2003;3:1859-1864.
4. Flemings MC. *Solidification Processing*. New York, NY: McGraw-Hill; 1974.
5. Kwauk X, Debenedetti PG. Mathematical modeling of aerosol formation by rapid expansion of supercritical solutions in a converging nozzle. *J Aerosol Sci*. 1993;24:445-469.
6. Helfgen B, Hils P, Holzknecht C, Türk M, Schaber K. Simulation of particle formation during the rapid expansion of supercritical solutions. *J Aerosol Sci*. 2001;32:295-319.
7. Debenedetti PG. Homogeneous nucleation in supercritical fluids. *AIChE J*. 1990;36:1289-1298.
8. Wallis GB. *One-Dimensional Two-Phase Flow*. New York, NY: McGraw-Hill; 1969.
9. Rantakyla M, Jantti M, Aaltonen O, Hurme M. The effect of initial drop size on particle size in the supercritical antisolvent precipitation (SAS) technique. *J Supercrit Fluids*. 2002;24:251-263.
10. Angus S, Armstrong B, de Reuck KM. *International Thermodynamic Tables of the Fluid State—Carbon Dioxide*. London: Pergamon Press; 1976.
11. Michels A, Sengers JV, Ver der Gulik PS. The thermal conductivity of carbon dioxide in the critical region. *Physica*. 1962;28:1216-1237.
12. Stoldt J, Brunner G. Phase equilibria in complex systems of palm oil deodorizer condensates and supercritical carbon dioxide: Experiments and correlation. *J Supercrit Fluids*. 1999;14:181-195.
13. Press WH, Teukolsky SA, Vetterling WT, Flannery BP. *Numerical Recipes*. 2nd Edition. Cambridge, UK: Cambridge Univ. Press; 1992.
14. Li J, Rodrigues M, Paiva A, Matos HA, Gomes de Azevedo E. Binary solid–liquid–gas equilibrium and its effect on particle formation from a gas-saturated solution process. Proc of 5th Brazilian Meeting on Supercritical Fluids. Florianópolis, SC, Brazil; 2004.

Manuscript received July 30, 2004, and revision received Dec. 7, 2004.